Eur. Phys. J. B **14**, 63–72 (2000)

THE EUROPEAN PHYSICAL JOURNAL B
EDP Sciences

Form-factor measurements on chromium with high-energy synchrotron radiation

J. Strempfer[1,a], Th. Brückel[2], W. Caliebe[2], A. Vernes[3], H. Ebert[3], W. Prandl[4], and J.R. Schneider[1]

[1] Hamburger Synchrotronstrahlungslabor HASYLAB at Deutsches Elektronen-Synchrotron DESY, Notkestrasse 85, 22603 Hamburg, Germany
[2] Institut für Festkörperforschung at Forschungszentrum Jülich, 52425 Jülich, Germany
[3] Institut für Physikalische Chemie, Universität München, Butenandtstrasse 5-13, 81377 München, Germany
[4] Institut für Kristallographie, Universität Tübingen, Charlottenstrasse 33, 72070 Tübingen, Germany

Received 17 August 1998 and Received in final form 10 August 1999

Abstract. Results of high-energy magnetic X-ray diffraction on pure antiferromagnetic chromium are presented. The temperature dependence of the propagation vector of the spin-density wave (SDW) and the strain-wave (SW) could be reproduced. The temperature dependence of the magnetic integrated intensity could be measured in the transversally as well as in the longitudinally polarised SDW phase. The magnetic form-factor has been determined in the transversally polarised SDW phase with five magnetic satellites. For the first time a spin-orbit separation has been performed by comparing X-ray to neutron data. The small orbital contribution to the magnetisation density turns out to be negligible, in agreement to our relativistic band-structure calculations. In addition, measurements of strain-wave reflections have been undertaken, and the results complement previous studies.

PACS. 75.25.+z Spin arrangements in magnetically ordered materials (including neutron and spin-polarized electron studies, synchrotron-source x-ray scattering, etc.) – 78.70.Ck X-ray scattering

1 Introduction

In recent years, in addition to non-resonant magnetic diffraction with hard X-rays (~ 8 keV photon energy), in the following denoted by "conventional X-ray diffraction", magnetic diffraction with photons in the energy range of 80 to 500 keV ("high-energy photons") has been developed on the model system $\mathrm{MnF_2}$ [1–4]. This method combines some advantages of both, neutron and conventional X-ray diffraction, such as bulk sensitivity and high momentum-space resolution. Here, we present a study of antiferromagnetic chromium, where results of both, high-energy X-ray diffraction and neutron diffraction, are taken into account. It is shown that the combination of these complementary probes with regard to magnetic diffraction gives a more complete picture than one method alone. This concerns in particular the separation of spin and orbital angular momentum. Such a separation has been undertaken with X-rays of conventional energies for ferromagnetic structures by Collins *et al.* [5] on $\mathrm{HoFe_2}$ and Laundy *et al.* [6] on Fe using a white-beam technique. For antiferromagnets such as Ho, UAs and NiO such a separation has been performed with X-rays in the medium-energy range using polarisation analysis [7–10]. In this paper, we present for the first time results for the separation of spin and orbital magnetic moments using a combination of high-energy X-ray and neutron diffraction. As a model system we chose antiferromagnetic chromium.

For magnetic diffraction with high-energy photons, the scattering cross section takes the following very simple form [4]:

$$\frac{\mathrm{d}\sigma}{\mathrm{d}\Omega} = r_0^2 \left(\frac{\lambda_\mathrm{C}}{d}\right)^2 |S_\perp|^2 , \qquad (1)$$

where r_0 is the classical electron radius, λ_C the Compton wavelength, d the lattice spacing and $S_\perp$ the Fourier transform of the spin component perpendicular to the diffraction plane. For neutron diffraction, the diffracted intensity is proportional to the combination $\mathbf{L}(\mathbf{Q}) + 2\mathbf{S}(\mathbf{Q})$ of both spin ($\mathbf{S}(\mathbf{Q})$) and orbital ($\mathbf{L}(\mathbf{Q})$) momentum. Thus, by combining the results of high-energy X-ray and neutron diffraction, orbital and spin contributions can be separated. We emphasise that the cross section given in (1) is polarisation independent. Therefore, polarisation analysis is not required for a measurement of the pure spin moment, in contrast to conventional X-ray diffraction. Other features of high-energy X-ray diffraction include the volume enhancement, where in contrast to non-resonant

---

[a] *Present address*: BESSRC-CAT at APS/ANL, 9700 South Cass Avenue, Argonne, IL 60439, USA
e-mail: `strempfer@anl.gov`

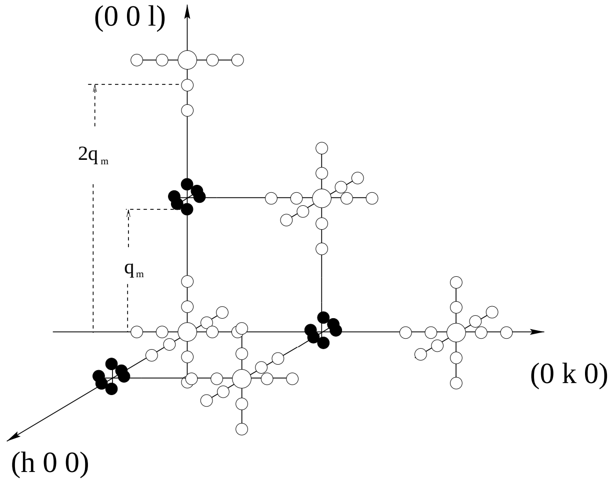

Fig. 1. Magnetic and strain-wave satellites in reciprocal space. First-order magnetic satellites are shown as full circles. First and second-order strain-wave satellites are shown as open circles. In addition, the main charge reflections are shown as large open circles. $\mathbf{q}_{\mathrm{m}}$ in reciprocal lattice units.

diffraction at medium energies, intensity is gained due to the small absorption, allowing the use of large samples.

Chromium is an itinerant antiferromagnet exhibiting an incommensurate spin-density wave (SDW) in the antiferromagnetic phase. The phase transition from the paramagnetic to the antiferromagnetic state takes place at the Néel-temperature $T_{\mathrm{N}} = 311$ K [11,12]. This SDW gives rise to magnetic satellite peaks at positions corresponding to the magnetic propagation vector $\mathbf{q}_{\mathrm{m}}$ of the SDW. The SDW has been explained by Overhauser [13] who relates the magnetic propagation vector $\mathbf{q}_{\mathrm{m}}$ of the SDW to the translation vector between electron and hole states in reciprocal space. $\mathbf{q}_{\mathrm{m}}$ describes the nesting vector between the respective two Fermi surfaces.

Above the spin-flip transition at $T_{\mathrm{SF}} = 123$ K, the SDW is transversally polarised, whereas below T_{SF}, the polarisation rotates to become parallel to the modulation wave vector which leads to a longitudinally polarised SDW [14].

Figure 1 shows the three-dimensional reciprocal space for chromium. The full dots represent the first-order magnetic satellites. $\delta = 1 - q_{\mathrm{m}} a / 2\pi$ denotes the distance from the first-order magnetic satellite to the next integral reciprocal lattice position. In the following, we will denote the satellites occurring at distances δ and their higher harmonics at 3δ as first and second-order SDW satellites. These reflections are found near extinct charge reflections of the fundamental bcc-structure.

Due to magneto-elastic coupling, the SDW is accompanied by an elastic strain-wave (SW) with a propagation vector of $2\mathbf{q}_{\mathrm{m}}$ [15]. The satellite reflections of this SW are found at distances of $n\,2\delta$ from the charge Bragg reflections. The first-order satellite reflections of this structure are situated at distances 2δ from ordinary charge reflections. We will denote these satellites as first- and higher-order SW satellites. These reflections are shown in Figure 1 as white circles. Often, these satellite reflections are also denoted as charge density wave (CDW) satellites. This is because both effects can contribute to diffraction at these positions in reciprocal space. A separation of SW and CDW is not easy and requires a very accurate determination of the satellite intensities. A separation of these effects has been attempted [16], but so far a CDW contribution could not be demonstrated unambiguously.

Up to now, first- and second-order magnetic satellites could be measured with neutron diffraction [17,18]. Also, the satellites due to the SW have been investigated extensively with X-rays [15,19]. Only satellites of first- and second-order have been found.

The measurement of magnetic reflections of chromium is difficult since the magnetic moment is very low. The amplitude of the magnetic moment amounts to $\mu = 0.62\mu_{\mathrm{B}}$ with a root mean squared moment of $\mu_{\mathrm{rms}} = 0.43\mu_{\mathrm{B}}$ [20].

Synchrotron X-ray measurements of the elastic SW have been performed by Gibbs *et al.* [19]. Non-resonant magnetic X-ray diffraction was reported by Hill *et al.* [21]. They investigated the temperature dependence of the wave vector $\mathbf{q}_{\mathrm{m}}$ and of the peak intensity of the magnetic $1+\delta\,0\,0$ satellite in the transversally polarised state of the SDW.

In this paper, we present a complete study of the Q-dependence of the SW and the SDW satellites. Since for high-energy X-ray diffraction geometric and absorption factors can be neglected, the intensities of the satellites could be determined to great precision. This is in contrast to conventional X-ray diffraction, and allows us to compare different models describing the interplay between SW and SDW based on a comparison of calculated and measured intensities. Because of the small divergence of the undulator beam and the resulting high resolution of the instrument even in the dispersive case, we were able to measure several points of the magnetic form-factor dependence up to a value of $\sin\theta/\lambda$ of more than 0.5 Å^{-1}.

The measurement of the ordered magnetic form factor with X-rays presented here represents the first measurement of higher order magnetic reflections on pure chromium in the antiferromagnetic state. Measurements of the magnetic form-factor of chromium have already been performed with neutrons. Moon *et al.* [22] have investigated samples of manganese doped chromium in the ordered antiferromagnetic state. In these samples, the SDW collapses to a commensurate antiferromagnetic state which eases the measurement. By varying the Mn concentration Moon *et al.* argue that the form-factor of these alloys is identical to the pure chromium form-factor. Measurements of the form-factor of the induced magnetic moment have been performed with polarised neutrons by Stassis *et al.* [23]. Recently we presented additional data [24]. By comparing to atomic Hartree-Fock calculations the form-factor of the ordered moment of chromium could be described by a pure spin dependence. The induced form-factor was described by 40% spin and 60% orbital form-factor.

The aim of the present investigation was to verify the pure spin nature of the ordered-moment form-factor by a model-independent method and search for possible solid state effects.

2 Experimental

The experiments were conducted at the high-energy undulator beamline PETRA II and at the high-field wiggler beamline BW5 at HASYLAB, Hamburg. As monochromator, we used an annealed Si-1 1 1 crystal with a mosaicity of $4''$ and a Ge-doped Si-1 1 1 crystal with a mosaicity of $20''$, respectively. Measurements have been performed in a two-crystal mode with monochromator and sample crystals, as well as in a three-crystal mode using an additional analyser crystal. In this case, the analyser crystal was of the same type as the monochromator crystal. The photon energy was 85 keV and 100 keV, respectively.

We used a cubic crystal with dimensions of $5 \times 5 \times 5$ mm^3. The crystal faces were cut to be 1 0 0- and 1 1 0-planes. Three crystallites were found with a mosaicity of $40''$ each. In a rocking curve scan, the reflections are separated by about $50''$. With a beam size of 1×1 mm^2 one of these crystallites could be isolated. The magnetic reflection observed at the $1-\delta\,0\,0$ position is shown in Figure 2. The count rate in the maximum is 60 counts/s above background at a ring current of 35 mA. The peak-to-background ratio is 6:1. The crystal was mounted with a $0\,1\,\overline{1}$ axis vertical in a He-cryostat, so that reflections of type $h\,k\,k$ could be observed. In this configuration, only satellites belonging to the $\langle 1\,0\,0\rangle$ domain could be measured. For the measurements of satellites of the $\langle 0\,1\,0\rangle$ and $\langle 0\,0\,1\rangle$ domains, a closed-cycle cryostat mounted in an Eulerian-craddle was used.

3 Band structure calculations

To support the interpretation of the experimental results presented below, band structure calculations for the commensurate antiferromagnetically ordered phase of chromium have been performed within the framework of spin density functional theory (SDFT) [26]. Because the magnetic properties of chromium depend extremely sensitive on the lattice parameter [27] it has been chosen 0.05% off from experiment to reproduce the experimental value for the magnetic moment (see above). The band structure calculations have been done with the spin polarised relativistic version of the Korringa-Kohn-Rostoker (KKR) method using the atomic sphere approximation (ASA) [28]. This approach gave access not only to the spin but also to the spin-orbit induced orbital magnetic moments. From the corresponding magnetisation density the spin and orbital magnetic form factors have been calculated on the basis of the dipole approximation [29,30]:

$$f_{\mathrm{spin}}(Q) = \int j_0(Qr) m_{\mathrm{spin}}(r) r^2 \mathrm{d}r / m_{\mathrm{spin}} \tag{2}$$

$$f_{\mathrm{orb}}(Q) = \int \left(j_0(Qr) + j_2(Qr)\right) m_{\mathrm{orb}}(r) r^2 \mathrm{d}r / m_{\mathrm{orb}}\,. \tag{3}$$

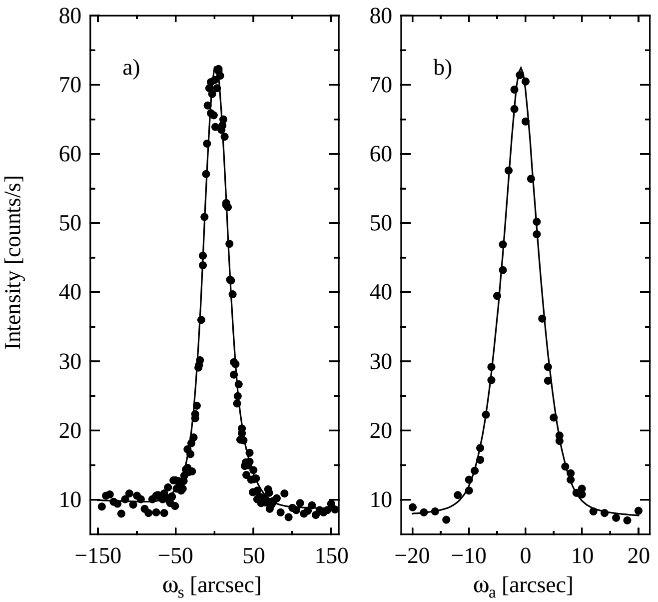

Fig. 2. Magnetic $1-\delta\,0\,0$-satellite at 135 K measured in the three crystal setup. (a) shows a rocking curve of the sample crystal, equivalent to a transverse scan. (b) shows a scan of the analyser crystal, which corresponds approximately to a longitudinal direction in reciprocal space [25].

Here $m_{\mathrm{spin}}(r)$ and $m_{\mathrm{orb}}(r)$ are the spin and orbital magnetisation, respectively, with the later determined by the orbital angular momentum density [30]. The quantities m_{spin} and m_{orb} are the corresponding spin and orbital magnetic moments. Finally, the functions $j_n(r)$ are the spherical Bessel functions of order n.

4 Magnetic form-factor

In chromium, conduction electrons carry the magnetic moment. Due to this delocalisation the form-factor falls off rapidly with increasing momentum transfer. For this reason, higher-order magnetic reflections are difficult to measure. To suppress background and increase the peak-to-background ratio, the form-factor measurements were performed in a three-crystal setup. We were able to measure five different magnetic satellites: $1{-}\delta\,0\,0$, $1{+}\delta\,0\,0$, $1{-}\delta\,1\,1$, $1{+}\delta\,1\,1$ and $1{+}\delta\,2\,2$. The peak intensities vary from 60 counts/s to 0.1 counts/s. Because of the divergence of the undulator beam of $\sigma = 2''$ and the imperfect monochromator and analyser crystals, the resolution of the instrument along the scattering vector was worse than the intrinsic width due to the distribution of the lattice parameter $\Delta d/d$, even in non dispersive setting. In this case, the FWHM of the analyser scan corresponds to the resolution along the Ewald sphere. To obtain the integrated intensity, we multiply the intensities of the rocking curve, measured in three-crystal setup, with the FWHM parallel to the scattering vector. A simulation has been performed to calculate the resolution width along the scattering vector of the very weak $1{+}\delta\,2\,2$ satellite, which could not be measured accurately. Here the information of the resolution function for the triple-axis diffractometer was used [25,31]. The calculated values for the width of

Table 1. Measured and calculated width of the analyser scan (ω_a) and calculated width in $q_{||}$-direction along the scattering vector.

Reflection	$\mathrm{FWHM}^\mathrm{meas}_{\omega_\mathrm{a}}$	$\mathrm{FWHM}^\mathrm{theo}_{\omega_\mathrm{a}}$	$\mathrm{FWHM}^\mathrm{theo}_{\lambda}$
$1{-}\delta\,0\,0$	7.9±0.2	8.0	8.1
$1{+}\delta\,0\,0$	7.2±0.2	7.4	7.5
$1{-}\delta\,1\,1$	13.8±0.5	13.3	13.3
$1{+}\delta\,1\,1$	15.0±0.7	14.3	14.2
$1{+}\delta\,2\,2$		32.9	35.1
0 2 2	31.2±0.7	30.5	32.0
2 2 2	39.0±1.0	38.4	42.6
4 0 0		44.3	51.7

Table 2. Mean value (scaled as in Fig. 3) and ratio of the form-factors of the magnetic satellites at temperatures of 125 K and 135 K around the positions 1 0 0 and 1 1 1 in reciprocal space. These values have been measured during several independent runs of PETRA and were found to be reproducible.

Position	T [K]	$\overline{f}_\mathrm{m}$	$f_\mathrm{m}^-/f_\mathrm{m}^+$
1 0 0	125	0.663±0.002	1.038±0.002
	135	0.663±0.003	1.038±0.006
1 1 1	125	0.374±0.004	0.978±0.009
	135	0.372±0.007	0.949±0.018

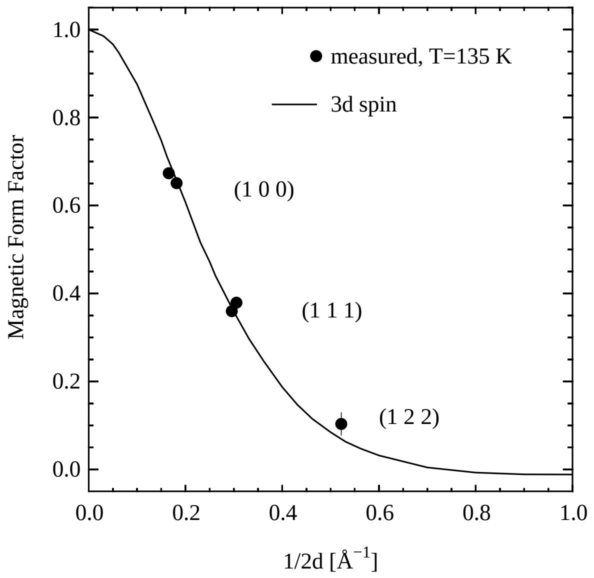

Fig. 3. Magnetic form-factor measured at the satellites $1{-}\delta\,0\,0$, $1{+}\delta\,0\,0$, $1{-}\delta\,1\,1$, $1{+}\delta\,1\,1$ and $1{+}\delta\,2\,2$ compared with the spherical atomic form-factor. The measured values are scaled to the calculated curve [32] which represents the spherical atomic form-factor for the $3d^4 4s^2$ configuration in Hartree-Fock approximation.

the analyser scan $\mathrm{FWHM}^\mathrm{theo}_{\omega_\mathrm{a}}$ and the width along the scattering vector $\mathrm{FWHM}^\mathrm{theo}_{\lambda}$ of the magnetic satellites and a few main charge peaks are tabulated together with the measured values in Table 1. Note the excellent agreement between measured and calculated values which justifies our procedure for the $1{+}\delta\,2\,2$ satellite. The magnetic form-factor is calculated from the integrated intensity (corrected for the temperature factor) as

$$f_\mathrm{m} \propto \sqrt{\frac{\sin 2\theta}{\lambda^3}\left(\frac{d}{\lambda_\mathrm{C}}\right)^2 I_\mathrm{int}} \propto \sqrt{dI_\mathrm{int}}. \tag{4}$$

Here, λ is the wavelength and θ the Bragg angle. We can determine only a relative form-factor dependence, since we did not measure the satellites for all three domains along $\langle 1\,0\,0\rangle$, $\langle 0\,1\,0\rangle$ and $\langle 0\,0\,1\rangle$. Our measurements show that an unequal population of the magnetic domains exists in our crystal, so that for an absolute measurement the intensity of all six satellites must be known. The form-factor determined for a sample temperature of 135 K at a photon energy of 100 keV is shown in Figure 3. For the 1 0 0 and the 1 1 1 satellites we can calculate the ratios of the satellite intensities. The ratios determined at sample temperatures of 125 K and 135 K are tabulated in Table 2. f_m^- and f_m^+ denote the form-factors of the satellite peaks at positions $1{-}\delta\,0\,0$ and $1{+}\delta\,0\,0$. To explain the differences in the form-factor between opposite satellites, two models are possible in the extreme case [11,33]. In the first model, the magnetic moment is assumed to be constant within one unit cell and to change the amplitude discontinuously to the next unit cell. It is described by the following modulation wave:

$$S^z = S_0^z \cos\left(\mathbf{q}_\mathrm{m} \cdot \mathbf{n}\right). \tag{5}$$

S_0^z is the maximum amplitude and $\mathbf{n}$ the vector to the edge of the unit cell. The magnetic form factors of the satellites are $f^- = f(\mathbf{G} - \mathbf{q}_\mathrm{m})$ and $f^+ = f(\mathbf{G} + \mathbf{q}_\mathrm{m})$, respectively. The ratio f^-/f^+ in that case is always greater than one.

In the other model the magnetic moment varies within the unit cell continuously. Here, the variation of the amplitude of the SDW is described by

$$S^z = S_0^z \cos\left(\mathbf{q}_\mathrm{m} \cdot (\mathbf{n} + \mathbf{r}_j)\right), \tag{6}$$

where $\mathbf{r}_j$ is the vector to the j-th atom. The ratio of the magnetic form-factors for the two satellites is in this case equal to unity, since the form-factors are both equal to that at the reciprocal lattice position $\mathbf{q} = \mathbf{G}$.

In the continuous model of the variation of the magnetisation amplitude, the SW can also be considered. It is described by

$$\mathbf{r}_j = \mathbf{r}_j^0 \pm \boldsymbol{\Delta}_2 \sin\left(2\mathbf{q}_\mathrm{m} \cdot (\mathbf{n} + \mathbf{r}_j^0)\right), \tag{7}$$

where $\mathbf{r}_j^0$ is the equilibrium position of the atom and $\boldsymbol{\Delta}_2$ the SW amplitude. Then the ratio of the magnetic form-factor is described by

$$\left(\frac{f_\mathrm{m}^-}{f_\mathrm{m}^+}\right)^2 \simeq (1 \mp 2\mathbf{G} \cdot \boldsymbol{\Delta}_2), \tag{8}$$

where the different signs originate form the phase shift of the SW relative to the SDW. The negative sign corresponds to the two waves in phase and the positive

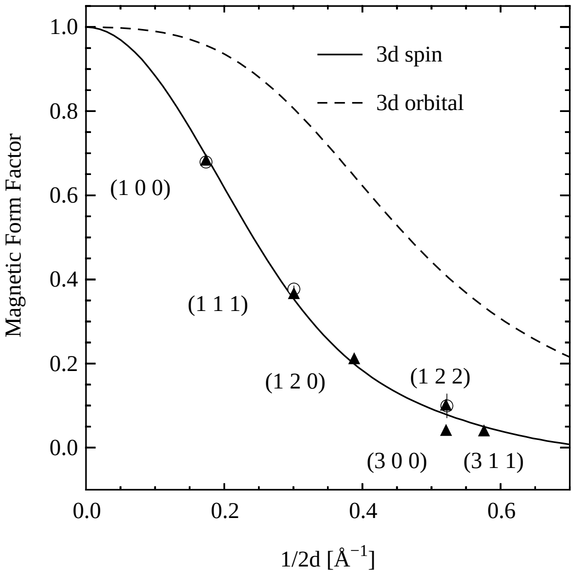

Fig. 4. Comparison of the mean values of the respective satellites around an integral position shown in Figure 3 (opencircles) with the neutron data of Moon *et al.* (full triangles) and the calculated curves for the pure spin form-factor and the pure orbital form-factor.

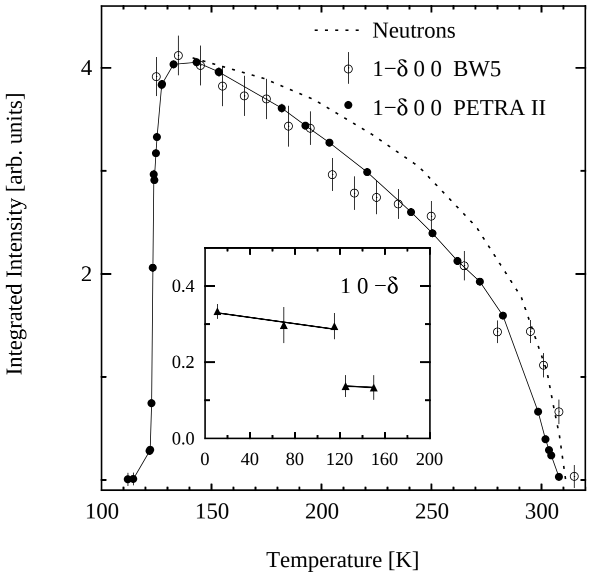

Fig. 5. Intensity of the magnetic $1-\delta\,0\,0$ satellite as a function of temperature. The inset shows the intensity of the $1\,0-\delta$ satellite below and above the spin flip transition. Full circles show results from the PETRA undulator beamline, open circles an additional measurement with poorer statistic taken on the BW5 wiggler beamline. The solid lines are guides to the eye. The dotted line represents neutron diffraction data [11].

sign describes the ratio with the two waves by π out of phase [35,12]. From this model, we expect the intensity ratio of the 1 0 0 and the 1 1 1 reflections to be the same after correction of the Debye-Waller factor, the magnetic form-factor and the Lorentz factor. This is not the case in our measurement (*cf.* Tab. 2). Instead, we see a ratio for f^-/f^+ which is larger than one for the 1 0 0 satellites and smaller than one for the 1 1 1 satellites.

In Figure 4, the mean values of the respective two satellites of Figure 3 are compared to results of Moon *et al.* [22]. The latter are neutron results measured on manganese-doped chromium crystals. Moon *et al.* showed that the form-factor of chromium does not depend on small manganese doping and they conclude that the form-factor given in [22] is characteristic for pure chromium. Within the error bars, neutron and high-energy X-ray data show the same behaviour.

The measurement of reflections lower in intensity than the (1 2 2) satellites, such as the (3 0 0) and (3 1 1) satellites, were made impossible by broad reflections at these positions arising from defect scattering. Since we are measuring at a level of 10^{-8} compared to the main charge reflections, we are very sensitive to this type of scattering which produced a temperature independent signal at certain positions in reciprocal space.

In Figure 4 also the theoretical spin and orbital magnetic form factors are plotted. For the spin magnetic form factor one finds it to be very similar to that derived from atomic wave functions (see Fig. 3). This means that for antiferromagnetically ordered chromium there are no pronounced solid state effects as it has been found before for the paramagnetic state, *i.e.* the induced for factor [34]. On the other hand, one notes that the spin and orbital form factors shown in Figure 4 are very different. One reason for this is that the spin magnetisation is somewhat more spread out in space than the orbital magnetisation. More important, however, is the fact that f_{orb} is, in contrast to f_{spin}, not only determined by the spherical Bessel function $j_0(Qr)$ but also by $j_2(Qr)$ (see Eqs. (3, 2)). The contribution to f_{orb} corresponding to $j_2(Qr)$ is zero for $Q = 0$ and shows a maximum for higher Q-values [30]. As a consequence f_{orb} of chromium decays much slower as a function of Q than f_{spin}.

The theoretical results given in Figure 4 allow to discuss the experimental form factor derived from the neutron and X-ray scattering experiments in a more detailed way. Assuming the X-ray data to stem only from the spin moment and using the calculated orbital form factor, the neutron data can be described by a superposition of the spin and orbital form factors with the orbital part contributing $-4(8)\%$. This is in reasonable agreement with the very small spin-orbit induced orbital moment of $-0.004\,\mu_{\text{B}}$ that has been obtained by the band structure calculation. It is interesting to note that the calculated orbital moment for antiferromagnetic chromium is about an order of magnitude smaller than that found for the pure ferromagnetic transition metals Fe, Co and Ni [28].

5 Temperature variation

Figure 5 shows the intensity of the magnetic $1-\delta\,0\,0$ reflection as a function of temperature. Here, the result of the very accurate measurement performed in the three-crystal mode at 100 keV is shown together with that of the measurement performed at 85 keV in two-crystal mode. It is clearly seen that the magnetic signal vanishes below

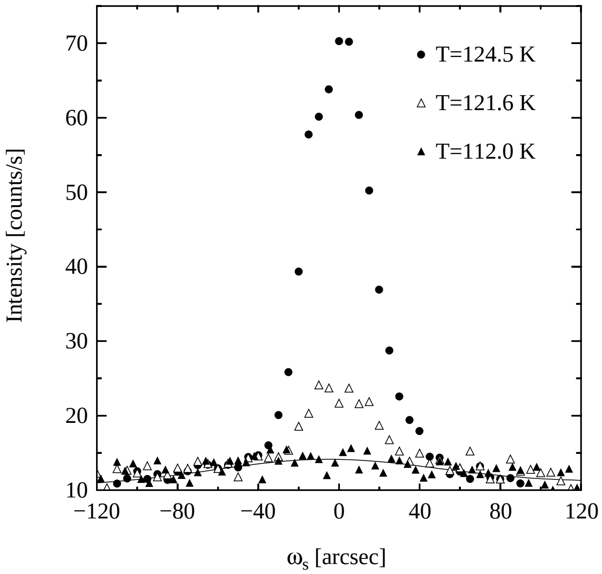

Fig. 6. Magnetic $1{-}\delta\,0\,0$-satellite at the spin-flip transition. The solid line shows a Gaussian fitted to the temperature independent background below T_{SF}.

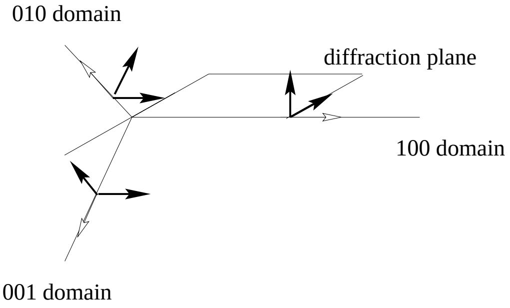

Fig. 7. Diffraction geometry with the three different propagation directions of the SDW along the main crystallographic axes. The black arrows indicate the six magnetic domains above T_{SF}, the open arrows show the directions of the magnetic moment below T_{SF}.

the spin-flip transition temperature $T_{\mathrm{SF}} = 123$ K. This is due to the form of the magnetic cross section (1). At the spin-flip transition, the polarisation of the SDW changes from transverse to longitudinal and the spin direction, which is perpendicular to the scattering plane above T_{SF}, comes to lie within the scattering plane below T_{SF}. In Figure 6, scans around T_{SF} are shown where the magnetic intensity vanishes within a temperature range of a few Kelvin. A temperature-independent broad background remains below T_{SF}. The inset of Figure 5 shows the intensity of the magnetic $1\,0\,{-}\delta$ reflection below and above T_{SF}. Here, the intensity is expected to change by a factor of two at the transition temperature if the domains with equal spin-propagation direction are equally populated [11]. This can be understood from the change of the spin direction in our diffraction geometry, as shown in Figure 7. Since the two domains with the same propagation vector in the transversally polarised phase are equally likely, a doubling of the volume with an inclination of the spin direction of 45° with respect to the diffraction plane is obtained by cooling through T_{SF}.

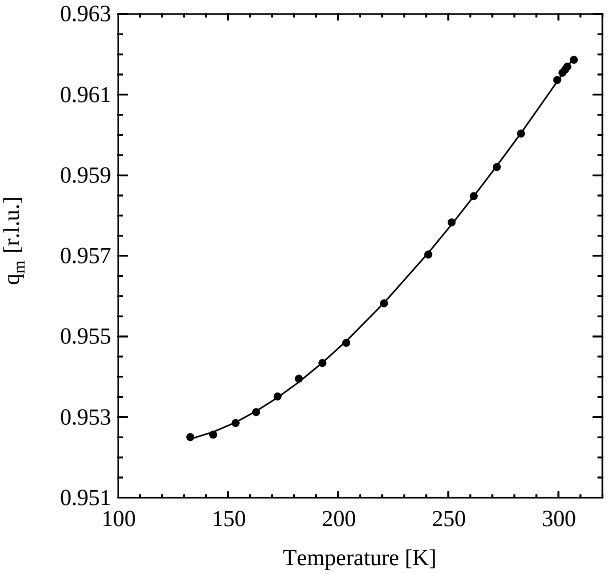

Fig. 8. Magnitude of the magnetic propagation vector in reciprocal lattice units as a function of the sample temperature measured at the $1{-}\delta\,0\,0$ satellite. The solid line is a guide to the eye to illustrate that the temperature variation is smooth.

We measure a change in intensity by a factor of 2.3 ± 1.3. Within our estimated standard deviation, the transverse domains are equally populated. The comparison of the intensities of the $1{-}\delta\,0\,0$ and the $1\,0\,{-}\delta$ satellite gives a very unequal population of these domains. A satellite of type $1\,\delta\,0$ could not be measured and is assumed to be again weaker than the $1\,0\,{-}\delta$ satellite. The population of the $\langle 0\,0\,1\rangle$ domains is found to be 8% of that of the $\langle 1\,0\,0\rangle$ domain. If we assume the occupation of the $\langle 0\,1\,0\rangle$ domain to be also 8% or smaller as compared to the $\langle 1\,0\,0\rangle$ domain, we can determine an occupation factor for the $\langle 1\,0\,0\rangle$ domains of $K = 0.86$ or more. A similar domain anisotropy has also been found by Hill *et al.* [21] and was attributed to stress induced by polishing, *i.e.* to near-surface effects. Here, we find that preferential domain population extends throughout the whole sample volume.

In Figure 8, the temperature dependence of the magnetic wave vector $\mathbf{q}_{\mathrm{m}}$ is shown. The smooth increase confirms the incommensurability of the magnetic period with respect to the period of the lattice.

6 Strain-wave

In addition to the magnetic satellites, satellites due to the SW induced by the SDW can be observed. The effects of SW and CDW are indistinguishable at first glance in our case. A separation is only possible if the charge formfactor is exactly known. Therefore it depends very much on the manner in which the form-factor is calculated. In the following, we denote the satellites caused by these two waves in the crystal lattice as SW satellites, since it turns out that the SW is the major contributor. We measured

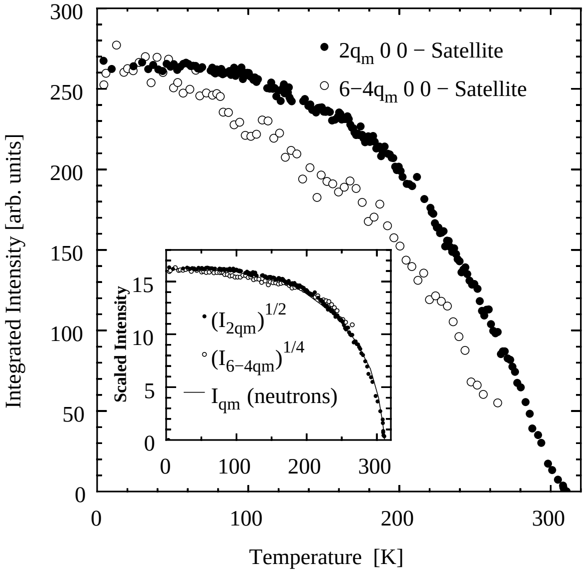

Fig. 9. Temperature dependence of the intensity of the first- and second-order satellites due to the SW. The full circles represent the values for the first-order SW satellite, the open circle show the intensity of the second-order satellite. The inset shows the scaled intensities. The solid line represents the intensity variation of the magnetic satellite measured with neutron diffraction [11].

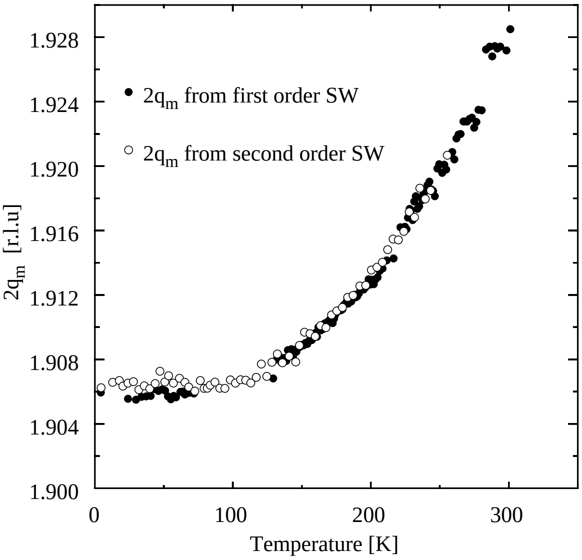

Fig. 10. Temperature dependence of the magnitude of the wave vector of the SW. The full circles represent the values for the first-order SW satellite, the open circle that of the second-order satellite. The solid line represents the temperature dependence of $2\mathrm{q_m}$ obtained from measurements at the magnetic satellite (see Fig. 8).

first- and second-order SW satellites. We searched for third-order satellites at positions $1-3\delta\,0\,0$ but could not observe any. The intensity as a function of temperature for the first- and second-order SW satellites is shown in Figure 9.

Landau theory predicts that the intensity of the satellite with wave vector $n\mathbf{q}_\mathrm{m}$ is proportional to $|\mathbf{M}_{q_\mathrm{m}}|^n$ for a sufficiently small amplitude of the SDW $|\mathbf{M}_{q_\mathrm{m}}|$ [36,17]. Therefore, the temperature variation of the appropriately scaled intensities should be identical. The inset of Figure 9 shows the scaled intensities as predicted by Landau theory. This behaviour could also be confirmed for the SW satellites by Hill *et al.* [21].

A comparison of these curves with the variation of the magnetic intensity in Figure 5 measured with high-energy X-rays shows that the temperature behaviour of the latter is different, whereas the intensity dependence obtained with neutron diffraction [17] follows the behaviour of the scaled SW intensities very well.

In Figure 10, the wave vector variation of the SW with temperature is shown. These measurements have been performed without an analyser, therefore the resolution along the scattering vector is moderate and amounts to $\Delta q_{||} \approx 0.02$ Å^{-1}. Within the accuracy of the measurement, the smooth variation found for $\mathbf{q}_\mathrm{m}$ in Figure 8 is confirmed.

In order to obtain the amplitude of the SW and to search for a possible CDW contribution, we measured the Q-dependence of the $2q_\mathrm{m}$ and the $4q_\mathrm{m}$ satellites at $T = 125$ K. The satellites around the $4\,0\,0$ reflections were measured at 100 keV in three-crystal mode to reduce the background for the weak second-order reflections. The relatively strong first-order $2\,0\,0$ satellites were measured at 85 keV in two crystal mode. An Fe-attenuator of up to 12 mm thickness was used for the measurement of first-order satellites because of the limited dynamical range of the detector. The integrated intensities were determined by correcting the transmitted intensities using the absorption factor taken from [37]. The main charge reflections were measured by attenuating the scattered signal by 42 mm Fe. The integrated intensities for the main charge reflections and the satellites are tabulated in Table 3. The three-crystal data have been treated in a similar way to the magnetic intensities. They were multiplied by the resolution width along the scattering vector, shown in Table 3, to obtain integrated intensities. The $2\,0\,0$ and $4\,0\,0$ main charge reflections have to be corrected for extinction and absorption of the attenuator. Since the magnetic reflections are extinction free and the lattice spacing for the $1-\delta\,0\,0$ of chromium and the Si-$1\,1\,1$ are almost the same, heading to non-dispersive setting, the extinction g-value can be calculated from the FWHM η of the magnetic satellite by using the relation $g = 1/(2\sqrt{\pi}\eta)$ if a Gaussian distribution is assumed [38]. The extinction has been corrected by using the Becker and Coppens extinction model [39]. Extinction factors of 4 and 1.56, respectively, have been determined. Whereas the intensities of the first-order SW satellites are almost identical, the second-order satellites show a significant difference in intensity. According to Overhauser [40], the ratio of the satellite intensities to the intensities of the main charge reflections can be described as follows:

$$\frac{I_{\pm n\mathbf{q}_\mathrm{m}}}{I_\mathbf{G}} \simeq K\frac{f(\mathbf{G}\pm n\mathbf{q}_\mathrm{m})}{f(\mathbf{G})}J_1^2\left[(\mathbf{G}\pm n\mathbf{q}_\mathrm{m})\cdot\boldsymbol{\Delta}_2\right] \qquad (9)$$

Table 3. Integrated intensities of the 2 0 0 and 4 0 0 main charge reflections together with the respective $2q_\mathrm{m}$ and $4q_\mathrm{m}$ satellites in the direction of the scattering vector at $T = 125$ K. The first-order satellites around the 2 0 0 reflection have been measured in two crystal mode, the first- and second-order satellites around the 4 0 0 reflection in three-crystal mode. FWHM_λ describes the width along the scattering vector. The intensities of the main charge reflections are corrected for extinction. The intensities of the 2 0 0 and 4 0 0 satellites were measured at different beamlines. They are not on an absolute scale and cannot be compared.

Reflection	FWHM_λ	I_int [arb. units]
$2q_\mathrm{m}\,0\,0$		$2.71(9) \times 10^5$
$2\,0\,0$		$4.56(10) \times 10^9$
$4–2q_\mathrm{m}\,0\,0$		$2.59(8) \times 10^5$
$4q_\mathrm{m}\,0\,0$	$47.9''$	$4.59(8) \times 10^1$
$2+2q_\mathrm{m}\,0\,0$	$49.8''$	$4.51(4) \times 10^5$
$4\,0\,0$	$51.7''$	$7.82(7) \times 10^9$
$6–2q_\mathrm{m}\,0\,0$	$53.2''$	$4.22(1) \times 10^5$
$8–4q_\mathrm{m}\,0\,0$	$54.8''$	$2.23(2) \times 10^2$

where $I_{\pm n\mathbf{q}_\mathrm{m}}$ and $I_\mathbf{G}$ are the intensities of the satellites and the main charge reflection, respectively, corrected for Lorentz- and Debye-Waller factor. $f(\mathbf{G} \pm n\mathbf{q}_\mathrm{m})$ and $f(\mathbf{G})$ are the corresponding charge form-factors, K represents the occupation factor of the domain under consideration, and $J_1[z]$ is the first-order Bessel-function. For the mean value of the satellite intensities, equation (9) can be approximated by

$$\frac{\overline{I}_{n\mathbf{q}_\mathrm{m}}}{I_\mathbf{G}} \simeq K \left(\frac{(\mathbf{G} \cdot \boldsymbol{\Delta}_2)}{2} \right)^2 . \qquad (10)$$

The relative distortion Δ_2/a due to the SW is determined from the two-crystal data for the satellites around the 2 0 0 position to be $\Delta_2/a = (1.3 \pm 0.4) \times 10^{-3}$. Here, we give only the estimated standard deviation for counting statistics. In addition there might be a systematic error due to the rather large extinction correction. The result of a direct comparison of the satellite intensities, as first done by Mori and Tsunoda [16], is shown in Table 4. In [16] a CDW with an amplitude of approximately 0.01 electrons/atom was proposed. However, with the form factor of [41] their and our measured ratios are consistent with a pure SW. A contribution of a CDW with an amplitude of 0.01 electrons/atom would result in a deviation from the value of a pure SW by 3.5%, which is not consistent with our findings at the 4 0 0 position. However, the calculated ratio itself is very sensitive to the calculated atomic form-factor.

The intensities of the second-order SW satellites also shown in Table 3, cannot be explained by the model where a simple sinusoidal modulation (7) is assumed. They differ by almost a factor of 5 whereas, according to the expression proposed in [16], the difference in intensity should be smaller than 50%. The average intensity of the second-order SW satellites measured around the 4 0 0 position can be compared with the average intensity of the first-order satellites, as has been done by Hill *et al.* [21]. To describe the intensity by an expression analogous to (10), a second Fourier component Δ_4 in (7) is necessary. The position of the j-th atom is then described by [21]

$$\mathbf{r}_j = \mathbf{r}_j^0 \pm \left\{ \boldsymbol{\Delta}_2 \sin\left(2\mathbf{q}_\mathrm{m} \cdot (\mathbf{n} + \mathbf{r}_j^0)\right) + \boldsymbol{\Delta}_4 \sin\left(4\mathbf{q}_\mathrm{m} \cdot (\mathbf{n} + \mathbf{r}_j^0)\right) \right\} . \qquad (11)$$

We find the ratio of these Fourier components to be $\Delta_4/\Delta_2 = (1.75 \pm 0.8) \times 10^{-2}$, which is in good agreement with the value of $(1.9 \pm 0.3) \times 10^{-2}$ determined by Hill *et al.*

Table 4. Measured intensity ratios of the SW satellites around the 2 0 0 and 4 0 0 position in reciprocal space compared with calculated values for a pure SW using the atomic form-factors of [41]. Additionally, the averaged values determined by Mori and Tsunoda [16] are shown.

Position	I^+/I^-		
	measured	calculated	measured [16]
2 0 0	0.96±0.04	0.918	0.909±0.010
4 0 0	0.94±0.01	0.934	0.932±0.015

7 Discussion

The principle experimental findings which require further discussion are:

- the precise determination of the temperature dependence of the magnetic propagation vector in the bulk and of the SDW intensities;
- the unequal population of the SDW domains;
- the intensity ratio of the SW satellites, which gives information on a possible CDW contribution;
- the intensity ratio of the magnetic satellites, which gives information on the spin density distribution throughout the unit cell;
- the separation of spin and orbital magnetic form-factor.

In what follows we will discuss each of these points in greater detail.

As for the temperature dependence a smooth variation of the magnetic propagation vector was found which indicates that the magnetic period is incommensurate to the period of the lattice at least for the transversally polarised SDW. This result is a complement to the result of Hill *et al.* [21] to avoid possible surface effects and to be able to make a statement for the crystal bulk using the high resolution of X-rays diffraction. Note that in rare earth metals like holmium [42] and erbium [43], which also have an incommensurate magnetic structure, a lock-in to commensurate positions for lower temperatures has been observed.

As can be seen in Figure 5, the X-ray intensity variation of the magnetic satellite with temperature differs from the curve determined by neutron diffraction. The behaviour found by Hill *et al.* [21] is very similar to the one found here although their measurement suffers of poor statistics. A possible explanation could be that the domain distribution among the two domains with equal propagation vector of the SDW changes with temperature. This cannot be detected by neutron diffraction because here both domains contribute equally if satellites of type $1 \pm \delta\, 0\, 0$ are investigated. In the case of high-energy X-ray diffraction the measured intensity depends on the component of magnetisation perpendicular to the diffraction plane. So, small changes in domain distribution of domains with equal propagation vector can have an effect on the measured intensity. The comparison between the intensity variations of the SDW and SW satellites, shown in Figure 9, confirms this assumption. Here, the neutron data coincide very well with the scaled intensity of the SW satellites.

We found very unequal populations of the 1 0 0 and 0 0 1 domains leading to the strong difference in intensity of the $1-\delta\, 0\, 0$ and the $1\, 0 -\delta$ satellites. This was also stated by Hill *et al.* [21]. They attributed it to near-surface effects. From our measurements with high-energy photons we can conclude that this effect extends throughout the whole crystal. A possible explanation for this behaviour could be the strain induced through the SW. It favours the formation of one domain, if the energy of producing a domain wall is larger than the magnetic energy. This very unequal domain population has been found also in a neutron diffraction experiment which we performed on a different sample. This confirms the assumption that it is a true bulk effect. However, the population of the two domains with equal propagation vector in the transversally polarised phase is likely to be nearly identical, as shown by the intensity variation of the magnetic satellite at T_{SF}. A small change in the distribution of these domains with temperature remains possible, as discussed above. Because of the large statistical error in case of the intensities from the $\langle 0\,0\,1 \rangle$ domain an unequal population of the two $\langle 0\,0\,1 \rangle$ domains in the transversally polarised SDW cannot be concluded.

We have measured the intensity ratio of the $2q$-satellites in an attempt to distinguish between a contribution of the SW and the CDW. It turns out that such a separation is difficult because the data evaluation is very sensitive to the atomic form-factor for the charge reflections. Different model calculations [41,44] will result in a different ratio between the CDW and the SW contribution. An effort of a separation has been undertaken by Mori and Tsunoda [16]. They state a small CDW contribution with an amplitude of 0.003–0.02 electrons/atom. However, Table 4 shows that their data is consistent with a pure SW, if the form-factor of [41] is used. Kugler [45] could determine that the amplitude of the CDW must be smaller than 0.001 electrons/atom. Our results differ slightly from the values found by Mori and Tsunoda and are consistent with a pure SW state for chromium. We conclude that the CDW contribution is negligible.

From the intensity ratio of the magnetic satellites a determination of the spin-density distribution throughout the unit cell can be deduced for the SDW. Werner, Arrot and Kendrick [11] found an intensity ratio at the 1 0 0 reflection of $I^+/I^- = 0.78 \pm 0.02$, significantly different from 1. Therefore they stated that the rigid-spin model is the appropriate model for chromium. In this model, the magnetic moment is assumed to vary discontinuously from one atom to the other. Our data for the 1 0 0 reflection are consistent with their interpretation. However, so far only data for the 1 0 0 position are published. Surprisingly we find an inverted ratio at the 1 1 1 position (see Tab. 2). Therefore a statement about the type of modulation from our measurements is critical. Since the ratio $(f^-/f^+ - 1)$ is positive for the 1 0 0 and negative for the 1 1 1 satellite, no definite phase relation between SDW and SW can be determined [35]. An investigation of magnetic satellites at more reciprocal lattice positions could give some hint how to chose the right model.

For the moment distribution in the ordered phase we have reported a separation of spin S and orbital L form-factor. Because of the form of the magnetic scattering cross section, a model independent separation is not possible with neutron diffraction alone. In contrast to neutron diffraction X-rays allow a L/S determination by employing polarisation analysis. Such measurements have been performed on Ho, UAs and NiO [7–10]. For chromium with its small magnetic moment these experiments present a real challenge, since diffracted intensities over 8 orders of magnitude have to be measured. Therefore we propose here a new method of combining high-energy X-ray and neutron diffraction, avoiding further intensity reduction due to polarisation analysis of the scattered beam. Taking the X-ray form-factor to be spin-only, we can deduce an orbital contribution of $-4(8)\%$ to the neutron form-factor. This is in reasonable agreement with the very small spin-orbit induced orbital moment of $-0.004\,\mu_{\mathrm{B}}$ which has been obtained by our band structure calculation. It is interesting to note that the calculated orbital moment for antiferromagnetic chromium is about an order of magnitude smaller than that found for the pure ferromagnetic transition metals Fe, Co and Ni [28]. Note that an antiparallel orientation of L and S is expected in a simple atomic picture for a less than half filled d shell according to Hund's third rule. The most severe systematic error for our experimental result stems from the fact that our X-ray data have not been measured on an absolute scale. Such a measurement is difficult due to the six domains in the SDW state. For this reason we had to rely on a calculated Q-dependence of the orbital angular-momentum form-factor. Clearly, this can lead to systematic errors and implies the large estimated standard-deviation of 8%. While we have demonstrated the method, it would be desirable to repeat the X-ray measurements on a manganese-doped chromium crystal where the magnetic satellites are concentrated in one commensurable peak, resulting in better statistics.

Due to the small absorption, transition metals are ideally suited for high-energy X-ray investigations. However, spin and orbital form-factor have a similar Q-dependence for $3d$ elements which renders a determination of L/S by the method proposed here more difficult. This is not the case for actinides. While the heavier rare earth $(4f)$

elements have more localised (atomic like) magnetic properties a separation of L and S would be of high interest for the lighter lanthanides ($4f$) and actinides ($5f$). Here, the Q-dependence of spin and orbital momentum differ considerably, but the high absorption cross section will lead to a smaller volume enhancement.

8 Summary

We were able to determine a form-factor dependence of pure chromium by measuring five satellite reflections. A comparison to neutron measurements on a manganese-doped chromium crystal [22], indicates a negligible orbital momentum contribution.

From the comparison of the temperature dependence of the magnetic intensity below and above the spin flip temperature we can assume an unequal domain occupation in the bulk of the sample for the SDW with equal propagation direction in the transverse polarised state.

For the SW satellites similar results to former investigations with conventional X-ray diffraction were found. A CDW contribution could not be established.

To conclude, we can say that high-energy synchrotron radiation is well suited to measure the magnetic form-factor of transition metals. Results are obtained even in case of a very small magnetic moment as it is the case for chromium.

We thank M. Blume and P.H. Dederichs for stimulating discussions and D. Hupfeld for his assistance with the experiment at BW5. This work was supported by the BMBF under contract number 03-BR4DES-2.

References

1. Th. Brückel, M. Lippert, R. Bouchard, T. Schmidt, J.R. Schneider, W. Jauch, Acta Cryst. A **49**, 679 (1993).
2. M. Lippert, Th. Brückel, Th. Köhler, J.R. Schneider, Europhys. Lett. **27**, 537 (1994).
3. J. Strempfer, Th. Brückel, U. Rütt, J.R. Schneider, K.-D. Liss, Th. Tschentscher, Acta Cryst. A **52**, 438 (1996).
4. J. Strempfer, Th. Brückel, D. Hupfeld, J.R. Schneider, K.-D. Liss, Th. Tschentscher, Europhys. Lett. **40**, 569 (1997).
5. S.P. Collins, D. Laundy, G.Y. Guo, J. Phys.-Cond. Matter **5**, L637 (1993).
6. D. Laundy, S.P. Collins, A.J. Rollason, J. Phys.-Cond. Matter **3**, 369 (1991).
7. D. Gibbs, D.R. Harshman, E.D. Isaacs, D.B. McWhan, D. Mills, C. Vettier, Phys. Rev. Lett. **61**, 1241 (1988).
8. D.B. McWhan, C. Vettier, E.D. Isaacs, G.E. Ice, D.P. Siddons, J.B. Hastings, C. Peters, O. Vogt, Phys. Rev. B **42**, 6007 (1990).
9. S. Langridge, G.H. Lander, N. Bernhoeft, A. Stunault, C. Vettier, G. Grübel, C. Sutter, F. de Bergevin, W.J. Nuttal, W.G. Stirling, K. Mattenberger, O. Vogt, Phys. Rev. B **55**, 6392 (1997).
10. V. Fernandez, C. Vettier, F. de Bergevin, C. Giles, W. Neubeck, Phys. Rev. B **57**, 7870 (1998).
11. S.A. Werner, A. Arrot, H. Kendrick, Phys. Rev. **155**, 528 (1967).
12. E. Fawcett, Rev. Mod. Phys. **60**, 209 (1988).
13. A.W. Overhauser, Phys. Rev. **128**, 1437 (1962).
14. J.M. Hastings, Bull. Am. Phys. Soc. **5**, 455 (1960).
15. Y. Tsunoda, M. Mori, N. Kunitomi, Y. Teraoka, J. Kanamori, Solid State Commun. **14**, 287 (1974).
16. M. Mori, Y. Tsunoda, J. Phys.-Cond. Matter **5**, L77 (1993).
17. R. Pynn, W. Press, S.M. Shapiro, S.A. Werner, Phys. Rev. B **13**, 295 (1976).
18. S. Iida, Y. Tsunoda, Y. Nakai, J. Phys. Soc. Jpn **50**, 2587 (1981).
19. D. Gibbs, K.M. Mohanty, J. Bohr, Phys. Rev. B **37**, 562 (1988).
20. A. Arrot, S.A. Werner, H. Kendrick, Phys. Rev. **153**, 624 (1967).
21. J.P. Hill, G. Helgesen, D. Gibbs, Phys Rev. B **51**, 10336 (1995).
22. R.M. Moon, W.C. Koehler, A.L. Trego, J. Appl. Phys. **37**, 1036 (1966).
23. C. Stassis, G.R. Kline, S.K. Sinha, Phys. Rev. B **11**, 2171 (1975).
24. J. Strempfer, Th. Brückel, G.J. McIntyre, F. Tasset, Th. Zeiske, K. Burger, W. Prandl, Physica B **267-268**, 56-59 (1999).
25. H.-B. Neumann, U. Rütt, R. Bouchard, J.R. Schneider, H. Nagasawa, J. Appl. Cryst. **27**, 1030 (1994).
26. S.H. Vosko, L. Wilk, M. Nusair, Can. J. Phys. **58**, 1200 (1980).
27. K. Hirai, J. Phys. Soc. Jpn **67**, 1776 (1998).
28. H. Ebert, P. Strange, B.L. Györffy, J. Phys. F **18**, L135 (1988).
29. G.Y. Guo, W.M. Temmerman, H. Ebert, Physica B **172**, 61 (1991).
30. M.M.S. Brooks, O. Erikson, L. Severin, B. Johansson, Physica B **192**, 39 (1993).
31. U. Rütt, H.-B. Neumann, H.F. Poulsen, J.R. Schneider, J. Appl. Cryst. **28**, 729 (1995).
32. A.J. Freeman, R.E. Watson, Acta Cryst. **14**, 231 (1961).
33. S.W. Lovesey, *Theory of neutron scattering from condensed matter* (Oxford University Press, New York, 1984).
34. K.H. Oh, B.N. Harmon, S.H. Liu, S.K. Sinha, Phys. Rev. B **14**, 1283 (1976).
35. Y. Tsunoda, Y. Nakai, N. Kunitomi, Solid State Commun. **16**, 443 (1975).
36. C.F. Eagen, S.A. Werner, Solid State Commun. **16**, 1113 (1975).
37. S. Brennan, P.L. Cowan, Rev. Sci. Inst. **63**, 850 (1992).
38. W.H. Zachariasen, *Theory of X-ray diffraction in crystals* (Dover Publications, Inc., 1945).
39. P.J. Becker, P. Coppens, Acta Cryst. A **30**, 129 (1974).
40. A.W. Overhauser, Phys. Rev B **3**, 3173 (1971).
41. E.N. Maslen, A.G. Fox, M.A. O'Keefe, in *International Tables for Crystallography* Vol. C, (1992), p. 476.
42. D. Gibbs, D.E. Moncton, K.L. d'Amico, J. Bohr, B.H. Grier, Phys. Rev. Lett. **55**, 234 (1985).
43. D. Gibbs, J. Bohr, J.D. Axe, D.E. Moncton, K.L. D'Amico, Phys. Rev. B **34**, 8182 (1996).
44. M. Diana, G. Mazzone, Phys. Rev. B **5**, 3832 (1972).
45. W. Kugler, *Bestimmung der inkommensurablen Verzerrungswelle des Antiferromagneten Chrom mit Röntgenbeugungsexperimenten*, Dissertation, Universität Tübingen, 1983.